Journal of Energy Storage 65 (2023) 107069

Contents lists available at ScienceDirect

Journal of Energy Storage

journal homepage: www.elsevier.com/locate/est

Research papers

# Failure and hazard characterisation of high-power lithium-ion cells via coupling accelerating rate calorimetry with in-line mass spectrometry, statistical and post-mortem analyses

Mark Buckwell [a,b,*], Charlie Kirchner-Burles [a,c], Rhodri E. Owen [a,b], Tobias P. Neville [a], Julia S. Weaving [a,b], Daniel J.L. Brett [a,b], Paul R. Shearing [a,b]

[a] Electrochemical Innovation Laboratory, Department of Chemical Engineering, University College London, London, UK
[b] The Faraday Institution, Harwell Science and Innovation Campus, Didcot, UK
[c] National Physical Laboratory, Teddington, Middlesex, UK

ARTICLE INFO

*Keywords:*
Lithium ion batteries
Mass spectrometry
Accelerating rate calorimetry
Thermal runaway
Onset
Mitigation

ABSTRACT

Lithium-ion battery safety continues to be an obstacle for electric vehicles and electrified aerospace. Cell failure must be studied in order to engineer improved cells, battery packs and management systems. In this work, the thermal runaway of commercially available, high-power cells is studied, to understand the optimal areas to develop mitigation strategies. Accelerating rate calorimetry is coupled with mass spectrometry to examine self-heating and the corresponding evolution of gases. A statistical analysis of cell failure is then conducted, combined with post-mortem examinations. The methodology forms a robust assessment of cell failure, including the expected worst- and best-cases, and the associated real-world hazards. Cells produce a highly flammable, toxic gas mixture which varies over the course of self-heating. Failure also produces particulate matter which poses a severe health hazard. Critically, the onset of self-heating is detectable more than a day in advance of full thermal runaway. Likewise, voltage drops and leaks are detectable prior to venting, highlighting the potential for highly effective early onset detection. Furthermore, the behaviour of the cap during thermal runaway indicates that ejection of material likely reduces the chance of thermal runaway propagation to neighbouring cells. These findings also emphasise that research must be conducted safely.

## 1. Introduction

Lithium-ion batteries offer a portable power source for a broad range of devices and transport applications [1]. Ultimately, in combination with green and sustainable energy generation, they provide a route to reducing the fossil fuel consumption of transport [2]. As we increase our usage of lithium-ion batteries, safety has rightly become a critical issue. Although failure events are rare, estimated around 1 in every 10 million cells [1], the risk is significant due to tens of billions of batteries entering the market every year [3]. Thus, while there is substantial motivation for the increased use of lithium-ion batteries in electric vehicles (EVs) and aerospace, their uptake continues to be hampered by concerns with operational lifetime and safety, i.e., reliability; some applications remain for which lithium-ion batteries are not safe enough.

Cell failure can occur in several ways, such as electrical (short-circuiting), thermal (overheating) or mechanical (impact or penetration). Typically, the result is a rapid, uncontrolled increase in temperature, known as thermal runaway. Ultimately, this process can lead to explosions, fires, and the release of toxic and flammable ejecta and gases [4,5]. For example, organic compounds in the electrolyte are highly flammable, and lithium salts in the electrolyte, as well as the binder materials, are known to produce hydrogen fluoride (HF), a highly toxic compound [2,6]. Other typical gas constituents include hydrogen ($H_2$), carbon monoxide (CO), carbon dioxide ($CO_2$), and a variety of hydrocarbons. These are primary safety concerns in EVs [7], and may present further challenges in emerging applications, in particular for meeting the higher demands of the aerospace sector [8].

The failure of a single cell can propagate through a module or pack [9,10], so the behaviour of individual cells is a necessary study, such that safety measures may be engineered at the cell level [11], as well as at the level of batteries and management systems [12–14]. Given that cell failure is such a rare event under normal operation, the process must

* Corresponding author at: Electrochemical Innovation Laboratory, Department of Chemical Engineering, University College London, London, UK.
*E-mail address:* markbuckwell@ucl.ac.uk (M. Buckwell).

https://doi.org/10.1016/j.est.2023.107069
Received 14 December 2022; Received in revised form 22 February 2023; Accepted 4 March 2023
Available online 12 April 2023

be accelerated instrumentally through abusive testing, as. By 'pushing' cells into failure, we may discern the most likely and worst-case scenarios, and better understand what the risks are to on users, associated systems and the environment. Comprehensive characterisation studies are critical in consolidating information for commercial decisions, which is an effective means of driving technological changes for the benefit of society.

Here, we present a novel safety characterisation suite on a commercial nickel-cobalt-aluminium (NCA) 21700 lithium-ion cell with a capacity of >4 Ah. This high-power cell is rated for continuous delivery of a high current, making it an excellent candidate for automotive and aerospace applications. We use accelerating rate calorimetry (ARC) to fail cells, coupled with in-line mass spectrometry to study the gases produced during the entire failure process (from the early onset of self-heating, through venting and thermal runaway). We perform a statistical analysis to discern the likely worst-case temperature and heating rates that may be observed for a cell during thermal runaway, as well as the portion of cell energy transferred to heating. We use visual inspection and X-ray computed tomography (CT) to study the external and internal structure of cells, which allows us to build a quantitative picture of how the cell vent and casing interact during failure. Finally, we use scanning electron microscopy (SEM) and energy-dispersive electron spectroscopy (EDS), coupled with airborne contaminant monitoring to comments on the toxic and carcinogen nature of the particulates produced by cells as a result of thermal runaway. Note that in this work we define thermal runaway as the cell self-heating at >100 °C/min.

We find that the study cell can self-heat for over 35 h before thermal runaway. This leaves more than a full day from the onset of detectable failure signals during which time mitigation strategies may be employed. We observe a broad range of gases released both during venting (electrolytes, hydrogen and carbon dioxide) and thermal runaway (electrolytes and their breakdown products, as well as aromatics and significant carbon dioxide and hydrogen). These products, expelled during failure, are combustible and toxic. In addition, the respirable metal particles which accompany them pose a severe carcinogenic risk, accompanied by the toxicity of surface organophosphorus and organofluoride compounds.

Cells often rupture severely, and we show evidence that this appears to be associated with vent clogging and the mass lost during thermal runaway. Our findings are relevant to cell design, in the context of strategies to better cope with failure, should it occur. Vent design solutions which facilitate material ejection during thermal runaway may are likely to have a mitigating effect on the propagation of thermal runaway in battery packs. Furthermore, our results contribute to the growing body of knowledge on the hazardous products of thermal runaway, which may be used to support the emergency services in dealing with cell failure scenarios in the real world.

## 2. Experimental

Thermal abuse testing was carried out in a Thermal Hazard Technology ES ARC. Nickel tabs were attached to the cap and base of the cell for electrical operation within the ARC, and the tabs attached to the potentiostat leads via ring terminals secured with nuts and bolts. Cells were orientated with the cap towards the bottom of the calorimeter, and all electrical connections were well-insulated with glass cloth sheathing and tape. Fresh cells were firstly charged to 100 % state of charge (SoC). For tests requiring a lower SoC, cells were subsequently discharged as required. Cell wraps and insulating cap discs were removed prior to testing. Heat-wait-search (HWS) tests were carried out in 2 °C steps from 60 °C, with a 40-minute wait time and self-heating onset sensitivity of 0.005 °C/min for 10 min. The thermocouple was attached midway along the body of the cell, covered with aluminium tape (to optimise sensitivity at low heating rates) and secured with glass tape. Prior to testing, the system was calibrated to a maximum drift of ±0.0025 °C/min in adiabatic mode of using a dummy cell (Supplementary Fig. S1). For heat ramps (i.e., non-HWS tests), cells were heated at a rate of around 2 °C/min from room temperature until thermal runaway occurred. In these tests, thermocouples were attached along the side of the cell near the cap, midway along the body, and near the base.

For gas analysis, cells were contained in a closed steel canister within the ARC, with a gas outlet line in order to divert produced gases to a mass spectrometer. Mass spectrometry measurements were conducted using a Hiden QGA quantitative gas analyser, with the data collected in MASsoft 10.

The heat capacity of the study cell was determined using a heating pad with the ES ARC operating in adiabatic (exotherm) mode. The 2.5 cm × 2.5 cm heater was placed on the side of a single cell, and an insulating cuff was placed around the same side to improve heat transfer to the cell. The calorimeter was heated to ≈30 °C and left to soak for 1 h. The heater was then used to heat the cell to ≈40 °C at 1.84 W, during which time the ARC maintained an adiabatic environment. This gave a temperature change of 10.45 °C over 6 min. Given a cell mass of 66 g, we therefore estimated the heat capacity, $C_p$ of the test cell to be 816 J/kgK (using Eq. (1), as discussed later). We note that this value may vary with temperature.

X-ray CT scans were carried out in a Nikon XT H 225. SEM and EDS data were collected using a Zeiss EVO 10 with an Oxford Instruments EDS. From EDS measurements on electrodes removed from fresh cells, we estimate that the anode active material composition is 93 % carbon and 7 % $SiO_x$ by weight. The cathode active material composition is a lithium nickel cobalt aluminium oxide (NCA), containing 41 % nickel, 0.7 % cobalt and 2 % aluminium by weight.

Particle monitoring was carried out using an RS PRO 5322 Data Logging Air Quality Monitor.

Data are presented using a bright/high contrast colour palette combination for colour-blindness [15], as well as a similar custom implementation [16].

## 3. Results and discussion

### 3.1. Coupled accelerating rate calorimetry and in-line gas analysis

We used ARC coupled with mass spectrometry to characterise the behaviour of the study cell during self-heating and thermal runaway. The test system schematic is shown in Fig. 1a. The cell was heated in 2 °C steps from 60 °C. At each step, the calorimeter guard heaters heated the cell until its temperature reached the setpoint, after which time the whole system was left to equilibrate for 40 min. Finally, the system would maintain an adiabatic environment for 10 min, and if the cell was measured to be self-heating by 0.005 °C/min or more then the calorimeter switched into tracking mode and maintained the adiabatic environment as the cell continued to heat. This mode would continue until the exotherm ended; for the tests reported here, this was at thermal runaway.

Fig. 1b shows a typical self-heating profile of a 100 % SoC cell, from an onset of 86 ± 1 °C. This is higher than some reports of NCA cells, in which un-sustained self-heating was observed as low as 40 °C [17] in the presence of an electrolyte combining ethylene carbonate (EC) and ethyl methyl carbonate (EMC). Other reports of lithiated carbon in the presence of an electrolyte (i.e., cell components, rather than full cells) combining EC and diethyl carbonate (DEC) give an onset of around 80 °C [18–20]. Further literature on electrolytes containing dimethyl carbonate (DMC) reports thermal stability up to 180 °C [7]. Our test cells were NCA; in contrast, at an onset sensitivity of 0.02 °C/min, NMC, LFP and LMO cells have shown onset temperature of around 90 °C [21,22], although NMC has also been found to have an onset near 150 °C [23], and LCO cells have demonstrated an onset anywhere from 80 °C [24] to 140 °C [25]. There is clearly a large onset variation between cells of nominally the same chemistry, so self-heating is likely to depend heavily on the specific electrolyte composition of the cell. We expect the electrolyte of our test cell to include a significant portion of DEC, based on

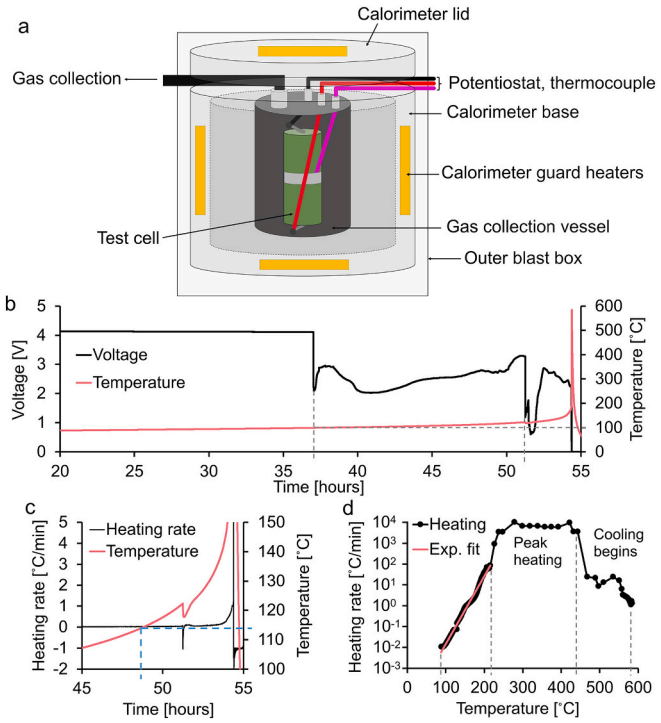


**Fig. 1.** ARC system schematic and heat-wait-search thermal abuse profiling of a 100 % SoC cell. a) ARC test schematic. The test cell is contained within a hermetically sealed steel gas collection vessel, with a gas collection outlet to the mass spectrometer and feedthroughs for the potentiostat and thermocouple. This vessel is placed within the calorimeter base, with the lid on top, and whole unit is surrounded by a protective blast box. b) Self-heating profile, from the onset at 86 °C, demonstrating distinct voltage drops while the cell self-heats over 35 h, until finally the voltage drops to 0 V as the cell goes into thermal runaway. Vertical markers at 37 h and 52 h indicate the voltage drops corresponding to SEI breakdown/separator softening and venting, respectively. Inset – expanded view of the shorting phase. c) Venting profile of the cell, demonstrating a small drop in temperature and negative heating rate as built-up gases are released from the cell. Blues markers indicate the temperature at which the cell reaches a heating rate of 0.02 °C. d) Self-heating profile of the cell, wherein there is an initial exponential dependence on the cell temperature. The cell continues to heat after the heating rate has reached a maximum (note that this is not a software/hardware limitation; we have recorded higher rates in other tests). Vertical markers denote the initial exponential phase, the peak heating phase, and the start of cooling.

the observed onset temperature at full charge. We also note that our ARC might not have been sensitive enough to detect self-heating at lower temperatures, below a heating rate of 0.005 °C/min.

The first distinct event during self-heating in Fig. 1a is the voltage drop at around 37 h. This most likely corresponds to the full breakdown of the solid electrolyte interphase (SEI) layer, which typically happens around 100 °C [26]. It is also possible that the separator has softened/weakened, without fully breaking down. No shorting has occurred as this point, as the voltage does not drop to 0 V. After another 15 h, the cell vents, correlating with a drop and subsequent recovery of the voltage; this is likely due to a temporary loss of connectivity between the cap and positive tab, or the triggering of the current interrupt device, which could have a similar effect [27]. Finally, between 54 and 55 h, the cell voltage drops to 1 V and then shorts to 0 V, leading to more rapid heating and a maximum temperature of 600 °C; this phase is shown more clearly inset in Fig. 1b. In another HWS test for a at 100 % SoC (as shown in Fig. 3), the maximum temperature observed was ca. 800 °C.

The venting at around 120 °C is shown more clearly in Fig. 1c, at which point the heating rate is briefly negative as the internal pressure from gas build-up is relieved. Thermal runaway finally takes place around 3 h after the cell vents. This is around 35 h after self-heating begins at a rate of 0.005 °C/min. The typical heating rate sensitivity used to determine the onset of self-heating of full cells in ARC testing is 0.02 °C/min [18,28–30], which we note would have only been reached once our cell reached around 115 °C, as indicated by the blue markers in Fig. 1c. This is only 3 h before venting, but is 29 h after we detected self-heating at 86 °C. We therefore emphasise the importance of conducting ARC at sufficiently high sensitivities to the self-heating onset temperature as soon as possible during HWS tests, with a high accurately. Otherwise, exothermic events may be missed, and the true behaviour of the cell improperly represented.

In the broader context of EVs and aerospace, early determination of self-heating, as we show here, would provide more than a full day to address a problem cell before it goes into thermal runaway. Furthermore, the occurrence of a voltage drop around 15 h before thermal runaway occurs might be useful in the context of mitigating or reducing the severity of cell failure. If a cell begins self-heating, and it is possible to detect either this or the voltage drop, then there is a significant window of time available to isolate the cell, make it safe, or otherwise remove it from operation.

The relation between the temperature and heating rate is shown more clearly in Fig. 1d. The first two vertical dashed lines denote a period of strong exponential correlation, from the onset of self-heating at 86 °C to thermal runaway at 227 °C. This onset is here defined as the point at which the heating rate exceeds an exponential dependence on temperature, at around 100 °C/min. Notably, similar exponential behaviour up to a heating rate of around 0.1 °C/min has been displayed by lithiated carbon heated in the presence of electrolyte [18], so we expect that these are the dominant active materials in this initial phase of self-heating, likely the start of SEI decomposition, which lasts until the cell reaches 100 °C. At a heating rate above 0.1 °C/min, as the cell approaches 150 °C, we would expect the separator to shut down and melt [27], such that Joule heating becomes dominant as the cell shorts [31]. We would also expect the carbonates in the electrolyte to readily decompose above 150 °C, particularly in the presence of lithium salt [32]. Subsequently for our test cell in Fig. 1d, the heating rate peaks at ca. 9500 °C/min and begins to decrease once the cell has reached around 450 °C, finally reaching a maximum temperature of 600 °C. We note that there might also be a heating contribution from any de-lithiated graphite [19] and from the nickel-containing cathode above 200 °C [26,33].

During the HWS testing shown in Fig. 1, we conducted in-line gas analysis. The mass spectrometer sampled continuously from 0.4 to 45 amu, taking around 15 s per spectrum. We sampled this broad range in order to get a full picture of the species present, and as such our data contained a large number of peak signals at integer amu values. However, each molecule present in the gas mixture produced a set of signals (a cracking pattern), and for many molecules (particularly hydrocarbons) these patterns overlap with one another in the expected mixture during thermal runaway (e.g., CO, ethylene, ethane). As such, it is not possible to decouple all the species present with mass spectrometry alone, so instead we selected particular *amu* signals to best describe the composition while accounting for overlapping peaks. The data are shown in Fig. 2, and have been normalised to the argon signal at 40 amu, which does not have an overlap and is taken to be at a constant background concentration. The other species with peak signals which do not suffer from an overlap in the expected gas mixture are $H_2$ (1 amu), $O_2$ (32 amu) and $CO_2$ (22 amu).

In Fig. 2a we see that around 45 min after venting, $CO_2$ is produced for around an hour, along with some quantity of $H_2$. Note that it is not possible to determine the true concentration of these species. $CO_2$ may have evolved at the cathode/electrolyte interface during the first charge, exacerbated by the subsequent heating during the HWS test [34], as well as from lithium-alkyl carbonate in the SEI layer above 120 °C [35]. Small quantities of $H_2$ may be produced by the reduction of the electrolyte within the graphite of the anode during lithium intercalation before/during SEI formation [34]. These signals then fall to baseline for

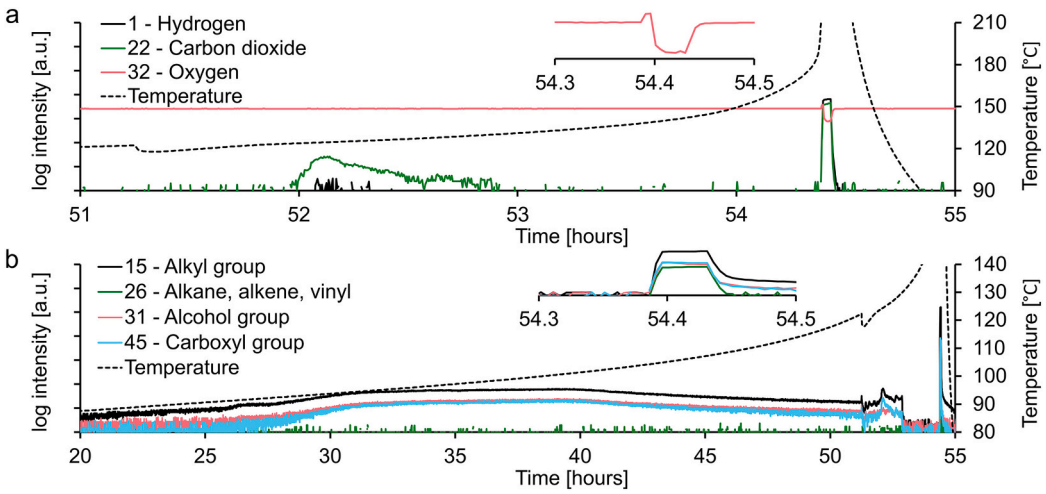


**Fig. 2.** In-line mass spectrometry of cell during HWS, corresponding to the test shown in Fig. 1. a) Venting and subsequent thermal runaway, showing the release of $H_2$ and $CO_2$ during both phases, and consumption of $O_2$ during thermal runaway. Inset – expanded view of oxygen signal during thermal runaway. b) Electrolyte appears to leak during self-heating, and some acids may be produced when the cell vents. During thermal runaway, further hydrocarbons are produced. Inset – expanded view of gases during thermal runaway.

another 1.5 h, before the cell enters thermal runaway. As the temperature exceeds 180 °C during thermal runaway, further $H_2$ and $CO_2$ are produced, in a significantly greater quantity. We also note that oxygen ($O_2$) is briefly released, likely from the electrolyte, before being consumed as the gases combust. $O_2$ might also be produced at the cathode if its temperature exceeds 200 °C [23].

Fig. 2b shows signals for hydrocarbon fragments at 15 amu (alkyl groups), 26 amu (alkane, alkene and vinyl), 31 amu (alcohol groups) and 45 amu (carboxyl groups) [36]. Here, we observe increasing signals at 15, 31 and 45 amu during self-heating once the cell has reached 90 °C, but no corresponding increase at 26 amu. This likely indicates that prior to venting, there is some leakage of electrolyte carbonates (EMC, DEC, DMC), which would produce significant signals at 15, 31 and 45, for example as a result of non-severe casing damage. This is in contrast to the presence of lighter hydrocarbons (e.g., methane, ethane, ethylene) which would be produced during combustion, with strong signals at 13 and/or 26 amu. We note that in other tests, including that of Fig. 3, we did not observe this leakage behaviour, so we are confident in attributing it to the cell rather than an artefact or the presence of some other material/contaminant in the system. Again, in the context of mitigating the hazards of thermal runaway, this leakage offers another potential signal that may be present very early on in the failure of the cell.

The leakage continues after the cell vents, with some fluctuation, before the signals appear to stop (they reduce down to the baseline/background level); at this point, no more electrolyte is leaving the cell. The long duration of leakage, particularly under heating, is likely to have driven off significant electrolyte vapour, though some may still be present as a liquid, for example in pores or other effectively sealed regions of the cell. We note that the boiling point of DEC is around 126 °C, which corresponds well with the vent temperature. Later we note the appearance of EMC in the Fig. 3, and this has a boiling point of around 108 °C. As mentioned above, we expect the electrolyte to contain significant DEC, so the loss of electrolyte signals following venting is reasonable. Finally, as thermal runaway occurs, we see strong peaks for each selected species, particularly at 15 amu, indicative of lighter hydrocarbons. The peaks at 31 and 45 also suggest the production of some alcohols (e.g., ethanol, methanol) and oxidised hydrocarbons (as evidenced by the carboxyl group signal). Importantly, we note that we did not detect any HF during this test. Given the signal range sampled (six orders of magnitude), this suggests that if any HF was produced, it would

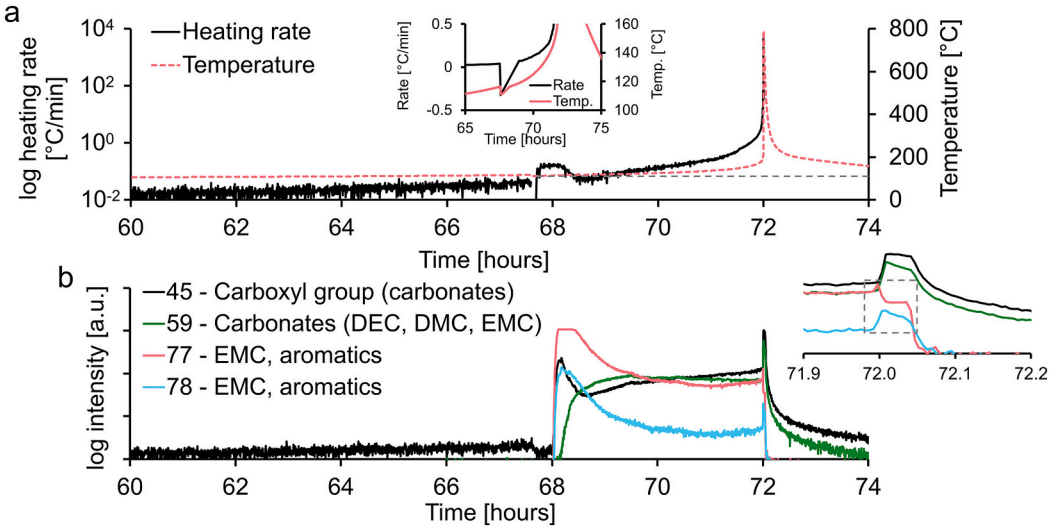


**Fig. 3.** Thermal/voltage and in-line mass spectrometry of cell during HWS, wherein the self-heating onset temperature was 91 °C. a) Voltage and temperature profiles demonstrating the voltage drop at around 53.5 h, venting at around 67.5 h and thermal runaway at 72 h. Inset – expanded view of the cell venting, showing the heating rate. b) Mass spectrometry of chosen *amu*, indicating the release of electrolyte, and production of aromatics. Note that due to data acquisition settings, the signal for 77 amu saturates just after 68 h, when the cell vents. Inset to right – expanded view of thermal runaway phase, highlighting difference between signals at 77 and 78 amu.

have been below 1 ppm. The 15, 31 and 45 amu signals returned to baseline by 56 h, so the gas emission time following thermal runaway was around 1.5 h, by which time the cell had cooled to below 40 °C.

To look for heavier species during failure of a cell at 100 % SoC, we carried out another HWS test under the same conditions, sampling from 43 to 80 amu, taking around 15 s per spectrum. Fig. 3a shows the temperature and self-heating profiles for the cell, including venting and thermal runaway. To best show these features, the full self-heating period is not shown; the cell began self-heating at 91 °C, 31.1 h into the test. We again observe venting when the cell reaches around 120 °C, followed by 4 h of self-heating prior to thermal runaway, with a peak heating rate of around $10^4$ °C/min.

Fig. 3b shows mass spectrometry signals for the test in Fig. 3a, corresponding to *amu* representing carboxyl groups at 45 amu (as would be present in carbonates), carbonate fragments at 59 amu (including each of DEC, DMC and EMC), and larger EMC fragments or aromatic rings at both 77 and 78 amu [36]. Note that for these data, no normalisation has been applied, as no appropriate signal was available. For this test, we did not observe significant leakage during self-heating, although there is a small increase in the signal at 45 amu from around 60 h that might indicate a lower degree of leakage than that shown in Fig. 2b. When the cell vents at 67.5 h, we observe strong peaks at 45, 77 and 78 amu, but only a gradual increase at 59 amu. The diversity of gases present makes the mixture difficult, perhaps impossible, to quantitatively analyse in-line using mass spectrometry. In particular, electrolyte carbonates should produce significantly larger signals at 45 amu than at 77 amu, and we should also see similar shape profiles at 59 amu. We therefore surmise that the carbonates have been severely degraded through interactions with each other and the lithium salt at high temperature. This would produce a variety of carbonate derivatives (e.g., alkyl carbonates, carbonate dimers) which are much heavier than the starting molecules, as have been previously reported from gas chromatography studies [37–41]. These products appear to leak out of the cell when it vents, while the heating rate is still relatively low (<1 °C/min).

As thermal runaway occurs in Fig. 3b, we observe strong peaks at all the selected *amu*. Most interestingly, the shapes of the peaks at 77 and 78 amu differ slightly. We interpret this discrepancy as resulting from the presence of aromatic hydrocarbons (e.g., benzene, styrene, o-xylene), which would produce a stronger signal at 78 amu than at 77 amu; conversely, the EMC signal should be stronger at 77 amu than at 78 amu. Aromatic species may be produced from cracking of hydrocarbons during thermal runaway [42], as well as from the breakdown of styrene-butadiene rubber if present as a binder, and have been detected previously in thermal decomposition studies of electrolyte mixtures [32]. The 45 amu signal returned to baseline at around 77 h, when the cell was still over 100 °C, so the gas emission time following thermal runaway was around 5 h, possibly as residual carbonates boiled off. The other signals returned to baseline by 73 h, so the emission time of heavier species following thermal runaway was around 30 min. This may have been due to residual gases in the sampling line taking some time to clear.

We note that we did not detect any fluorine–containing species (e.g., from PVdF or $LiPF_6$ breakdown in the electrolyte, as have been reported previously [43,44]), which have a number of peaks in the range 43–80 amu [36,45], i.e., if any were present then they were at <1 ppm. Our observations from mass spectrometry indicate that the gases vented from cells are a mix of $H_2$, $CO_2$ and a range of hydrocarbons. Carbon monoxide is also likely produced, although it was not possible in this instance to decouple its signal from the other species present. Altogether, this mixture is highly flammable, and although we did not detect any HF in this instance, carbon monoxide and aromatic hydrocarbons are toxic.

### 3.2. Statistical analysis of thermally induced failure

To study the effect of charge on failure, we use the ARC to conduct heat ramps on cells at a range of SoCs; 5 %, 17 %, 22 %, 27 %, 40 %, 57 %, 60 %, 75 %, 88 % and 100 %. Thermocouples were attached to the casing near the cap, half-way along the body, and near the base, to look at the heat distribution across the cell. Fig. 4 shows the effect of SoC on the failure dynamics. Interestingly, in contrast to other reports on NCA, LFP [46] and NMC [47] cells, we do not observe that the maximum measured temperature increases with SoC. Rather, for our study cell the temperature is lowest at around 60 % SoC. As mentioned above in relation to the HWS test self-heating onset temperature, this may be due to the specific electrolyte composition of our study cell.

We observe that the maximum heating rate increases exponentially with SoC, as shown in Fig. 4b, which is an agreement with other reports on NMC cells [47]. Our observations suggest that the stored energy which transfers to heating our study cell during thermal runaway does not depend strongly on the stored charge. However, the heating power does; energy is released more quickly at higher SoC. This is likely to be because more Joule heating occurs when the electrodes short at high SoC due to the greater stored charge available, which would have a pronounced accelerating effect on other reactions. We clarify here that the thermocouples are likely not to have captured higher-temperature flames or jets from the cell, and that we are not here considering any transfer to kinetic energy of ejecta.

We compared the temperatures at which venting and thermal runaway (i.e., the maximum heating rate) occurred, as shown in Fig. 4c. The venting temperature does not appear to be dependent on the SoC, and typically occurs around 180 °C. This is reasonable, given that the venting mechanism is engineered to occur at a pre-determined pressure; for a fixed quantity of gas in a fixed volume, this would be equivalent to a temperature dependence. If the vent mechanism is pressure-sensitive, then this suggests that the evolution of gases within the cell prior to thermal runaway is not dependent on the SoC. We note that the vent temperature here is around 60 °C higher than that observed during HWS testing. Thus, another possible explanation is that the venting mechanism is dominated by high temperature effects (i.e., the pressure increases according to the ideal gas law) rather than the pressure from gas evolution at lower temperatures. The strong dependence of the thermal runaway temperature on SoC might again be an indicator of the greater effect of Joule heating at higher states of charge, and has been similarly reported elsewhere for NCA cells [46]. The electrodes will be able to

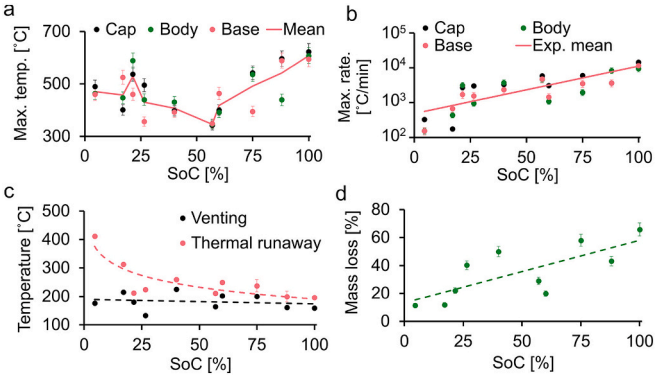


**Fig. 4.** Failure dynamics at SoCs of 5 %, 17 %, 22 %, 27 %, 40 %, 57 %, 60 %, 75 %, 88 % and 100 %. a) Maximum recorded temperature, which does not show a strong correlation with SoC. The solid line shows the cell temperature as the mean of the cap, body and base at each SoC. b) Maximum heating rate, which appears to depend exponentially on the SoC; the mean heating rate per SoC has here been fitted with an exponential function to highlight this correlation. c) Venting and thermal runaway temperatures, which respectively show no change with SoC, and a logarithmic dependence. Linear and logarithmic fits have been used here to highlight each relation. d) Mass loss, wherein there is a reasonably linear dependence on SoC, as shown by the fitted line. Note that we are not fitting here in order to model the behaviour, but to highlight correlations (or the lack, thereof) between parameters.

short when the separator breaks down, which will be a temperature-dependent process and typically occurs above 150 °C [27]. Therefore, the heating rate accelerates more quickly following separator breakdown at higher SoC as there is more charge stored to cause heating.

Fig. 4d demonstrates that more cell mass is lost at higher SoC, with a reasonably linear correlation. As such, we would expect higher SoC cells to eject heavier pieces of electrode assembly, or larger agglomerates of melted metals. As we noted in relation to Fig. 4a, the energy transferred to heating the cell does not appear to depend on SoC. So, the additional thermal runaway energy we would expect to see for higher SoC is likely transferred to kinetic energy, ejecting the cell contents. Previous reports have also shown that more violent thermal runaway events tend to be associated with the ejection of larger masses of material [48].

To carry out a statistical analysis of failure metrics, namely temperature, heating rate and mass loss, we carried out heat ramps on nine cells at 100 % SoC. Thermocouples were attached near the cap, midway along the body, and near the base of the cell. These tests were used to calculate reasonable mean and standard deviation values with which to generate normal distributions. This is a similar approach to the statistical analyses performed using fractional thermal runaway calorimetry data [48]. Eight heat ramps were conducted, along with one HWS without gas collection (i.e., the cell was not contained in the steel canister); this served as a control test, to confirm that the maximum temperature, heating rate and mass loss for a HWS was in general agreement with a heat ramp. Table 1 shows the failure metrics for the control cell, along with the means and standard deviations used to produce the distributions. The control cell values are generally within one standard deviation of the mean values, aside from the body maximum temperature, which is slightly low, and the cap and base heating rates, which are slightly elevated. Given that the standard deviations are, in general, quite large, we surmise that the behaviour of the control cell is within the normal variation exhibited by the cells. Therefore, the metrics for heat ramps and HWS tests are reasonably comparable.

The distributions for the maximum temperature measured by each thermocouple are shown in Fig. 5a. For each location on the cell, the distribution is centred around 600 °C. The tails of the distributions indicate that in rare cases we should expect to measure temperatures as low as 250 °C, or as high as 1000 °C. The cap is likely to show the highest temperature, while the body has a wider distribution at slightly lower temperature. The base is similarly shaped to the cap distribution, but at centred at a slightly lower temperature. Otherwise, the distributions are rather similar, which suggests that the cell heating is fairly evenly distributed across its length. For the heating rate in Fig. 5b, the cap shows a greater likelihood of heating more rapidly than the rest of the cell, although this distribution has a very large spread, with an expected worst-case heating rate of around 50,000 °C/min. This indicates that the behaviour of the cap is perhaps unpredictable during failure, as there may be effects from venting, ejecta, plasma jets, etc. Notably, at very high temperatures and heating rates the chance of thermal runaway propagation to a neighbouring cell within a battery pack would be greatly increased. So, it is clear from these distributions that such potential rare but extreme events should be considered in the design of thermal runaway mitigation strategies.

Fig. 5c shows the mass loss distribution from cells thermally abused at 100 % SoC, centred around 35 g. This is 54 % of the initial cell mass and agrees with what we would expect to see for cells at above 80 % SoC

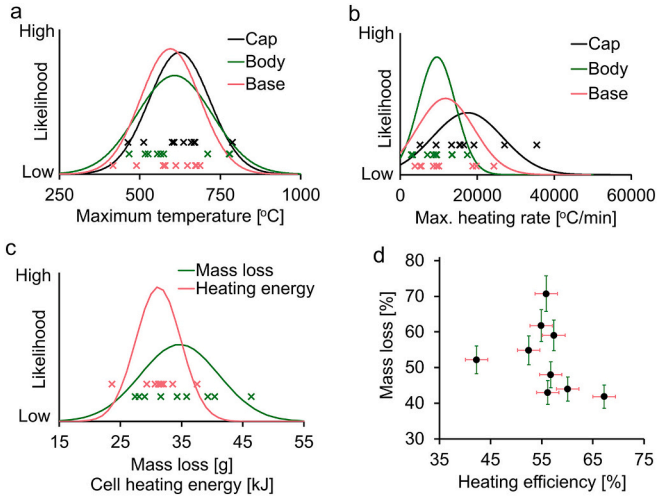


**Fig. 5.** Thermal abuse statistical analysis for nine cells at 100 % SoC undergoing thermal abuse. The cross symbols in a to c are used to mark the peak temperature values for each individual test used to produce the associated distributions. Their position in the vertical direction is arbitrary. a) Maximum temperature measured at the cap, body and base of cells. The cap typically gets slightly hotter than the rest of the cell. b) Maximum recorded heating rate at the cap, body and base of cells. The cap tends to heat most quickly, and the body most slowly. c) Mass loss and estimated heating energy during thermal runaway, centred around 35 g and 31 kJ, respectively. d) Percentage mass loss as a function of percentage heating efficiency, suggesting that there is not a strong correlation between the two. The error bars show the standard error.

from Fig. 4d. It is of note that the NCA cells we tested show similar peak temperatures to NMCs undergoing heat ramps [49]. We used these data in combination with the data in Fig. 5a and the self-heating onset temperature from the HWS test in Fig. 1 to estimate the total energy, $Q_{Heating}$, that heats the cell during thermal runaway. Assuming an onset temperature of 86 °C, the maximum cell temperature for each test provides an expectation of the total self-heating that the cell would experience during thermal runaway. The difference between these values provides $\Delta T$ in the specific heat capacity equation:

$$Q_{Heating} = m.C_{p}.\Delta T \quad (1)$$

where $m$ is the initial mass of the cell, typically 66 g. The resulting distribution, shown in Fig. 5c, is centred around 31 kJ. Importantly, this is only about 50 % of the total energy stored by the cell, which is around 60 kJ.

The residual energy not accounted for, around 30 kJ, is most likely attributable to the thermal runaway ejecta, both as thermal and kinetic energy, although it is beyond the scope of this paper to fully decouple the contributions of each. This is in agreement with other observations of the total energy carried by the cell ejecta [48]. In Fig. 5d we plot the heating efficiency (i.e., the percentage of the total cell energy heating the cell) against the percentage of mass lost. It might be expected that cells showing greater heating efficiency would demonstrate lower mass loss as more material, and thus energy, is retained in the cell. However, we do not observe any correlation between the cell heating energy and the mass loss during thermal runaway.

**Table 1**
Comparison of HWS control cell metrics with distribution means and standard deviations.

| | Maximum temp. [°C] | | | Maximum heating rate [$10^3$ °C/min] | | | Cell mass loss % | Heating efficiency % |
|---|---|---|---|---|---|---|---|---|
| | Cap | Body | Base | Cap | Body | Base | | |
| Control | 607 | 467 | 647 | 35.5 | 13.5 | 19.8 | 59 | 57 |
| Mean | 632 | 608 | 595 | 17.5 | 9.5 | 11.7 | 53 | 56 |
| St. dev | 94 | 117 | 92 | 9.1 | 4.8 | 7.4 | 10 | 7 |

### 3.3. Post-mortem characterisation of cell carcasses and debris

We studied the carcasses of all the cells thermally abused in this work, and observed a range of resulting failure modes that were readily distinguished by eye. These included:

i) Material stuck in the cap during ejection, in some cases associated with the presence of large chunks (ca. 13 g) of electrode assembly found in the failure debris. In these cases, no ruptures were present in the cell casing, as material was able to eject easily.
ii) Cap ruptures, sufficiently severe to allow material to escape the cell.
iii) Sidewall ruptures, typically when the cap did not fully open or rupture to allow material to eject from the cell.
iv) Bottom ruptures with or without the presence of other rupture, but typically with the cap intact, preventing material from leaving.

We collated the frequencies for which features appeared on the carcasses of thermally abused test cells in order to determine whether any correlations were present. In total, 29 cells were used to generate the appearance frequencies shown in Table 2, i.e., the percentage of cells showing the named feature. As may be seen here, the study cell has a high propensity for cap opening, stuck ejecta and bottom ruptures, with sidewall and cap ruptures also seen in multiple cells. Note that we are considering a cap to be open only in the case that a hole as wide as the central button is present, i.e., large enough for ejecta to readily exit through (an example is as shown in Fig. 7g).

We recorded the number of cell carcasses presenting each distinct pair of features as listed in Table 2. This provided a correlation value, wherein 100 % indicates that the correlating feature was always seen when the feature of interest was present, and 0 % indicates that they were never observed together on the same carcass. The results of this process are shown in Fig. 6a, which demonstrates that some failure features show a very strong correlation, and many show no correlation at all. Sidewall ruptures are always accompanied by bottom ruptures, and stuck ejecta always requires an open cap (correlation of 100 %). Conversely, when a bottom rupture is present, it is rare that a sidewall has also occurred (correlation of 20 %). Interestingly, an open cap typically results in stuck ejecta (correlation of 80 %), which likely indicates that the ejection process usually forces the cap open. The cap is also never open when cap ruptures occurred, and ejecta were never stuck when there was a sidewall rupture (correlation of 0 %). These observations altogether suggest a strong interplay between the behaviour of the cap venting/opening mechanism and the release of material from the cell. In particular, this suggests that the cap does not readily open to allow material to eject, whether by design or otherwise, and when it does open, ejecta still cannot readily leave the cell. As a result, during thermal runaway, energy may be confined to the cell, causing severe ruptures that could cause propagation of thermal runaway to neighbouring cells in battery packs.

We expect that vent clogging has an important role in the effectiveness of the cap opening and material ejecting. Clogging has previously been observed in correlation with case ruptures [50], so in order to further examine this behaviour, we used X-ray CT to probe the interior of the cell carcasses. Selected projections of the CT data are shown in Fig. 6b to g, demonstrating the presence of agglomerated, dense material on the inside of the cell cap for cells that showed severe rupturing. This is indicative of the cap becoming blocked during cell failure, leading to more material being retained in the cell during thermal runaway. Most likely, the blockage is melted aluminium from the cathode current collector, forced towards the cap under the high internal cell temperature and pressure. The cell surface temperature below 660 °C, as shown in Table 1 and Fig. 5, but previous work has shown that the internal temperature during thermal runaway can be as much as 400 °C higher than the surface [51]. So, we would certainly expect some aluminium to be present, and possibly even some copper, although we often large pieces of intact copper current collector in the cell debris, or within the cell carcass. These observations lead us to suggest two aspects of thermal runaway behaviour that might warrant further investigation. Firstly, whether it is critical that there is not so much melted aluminium present that it prevents the cap from being forced open ejecta. Secondly, and alternatively, that it may instead be critical that sufficient aluminium melts and accumulates to form a mass large enough to open the cap and make way for the ejecta. Notably, in the debris of failed cells, we often found a large deposit of solid aluminium (a few g), in many cases stuck to the wall of the calorimeter.

When the vent is clogged during thermal runaway, the energy contained within the cell must dissipate by another route, resulting in sufficient heating to melt the cell casing and cause ruptures. Indeed, in Fig. 6g we can see accumulated dense material around the inside of the sidewall rupture, which suggests the casing has melted rather than being forced open mechanically. When a rupture is sufficiently large, such as near the cap where there is some structural inconsistency and/or weakness due to the crimping, ruptures can be severe enough to allow the majority of the electrode assembly to eject. Retention of material in the cell is thus a significant risk for neighbouring cells in a battery back, due to the possibility of thermal runaway propagation via the extremely hot jets that produce ruptures. Furthermore, any material that does not eject from the cell becomes available as fuel for combustion, potentially prolonging the failure process and again increasing the chance of propagation to neighbouring cells. This highlights the importance of getting material away from neighbouring cells via effective ejection during thermal runaway.

Given our observations on the impact of cap opening on thermal runaway, we would expect a correlation between the mode of failure (the appearance of the features in Fig. 6a) and the mass lost from the cell as a result of failure. Interestingly, there appears to be a qualitative correlation when we examine the carcasses of abused cells, as shown in Fig. 7. Lower mass loss generally correlates with sidewall and large bottom ruptures (Fig. 7a, b and d), and higher mass loss correlates with open caps (Fig. 7g) and cap ruptures (Fig. 7i), i.e., ruptures as clear weak points in the cell casing. It is also of note that lower mass loss shows a slight correlation with higher peak temperature and rupturing, which again fits our supposition that expelling material may be beneficial in reducing the likelihood of thermal runaway propagation. However, our photos of the cell carcasses also highlight the intrinsic variation in the end result of cell failure. Some carcasses do have an obvious fit to our suggested trend, with cells showing no significant damage at both low and high mass loss (Fig. 7c and h), ejecta becoming stuck in the open cap of a cell with a low maximum temperature (Fig. 7e), and small bottom ruptures (Fig. 7f). In these cases, it is not clear why cells that have ejected little material do not also rupture, or how cells are able to eject significant material without their cap opening or any significant damage occurring. We also note, conversely, that other reports have demonstrated the inverse behaviour in 21700 cells, i.e., ruptures and severe damage being associated with lower peak temperatures [9] (these cells showed a similar propensity for rupturing/damage as our cells, with such events occurring in 9 % of tests). Nevertheless, it seems worthwhile to focus future studies on facilitating the ejection of material during failure as means of mitigating ruptures and failure propagation in battery packs.

**Table 2**
Carcass feature statistics for all 29 cells tested in relation to this work (i.e., including cells whose data are shown in all previous figures, as well as cells whose data have not been included).

| Feature type | Open cap | Ejecta stuck | Sidewall rupture | Cap rupture | Bottom rupture |
|---|---|---|---|---|---|
| Appearance frequency | 38 % | 31 % | 7 % | 7 % | 38 % |

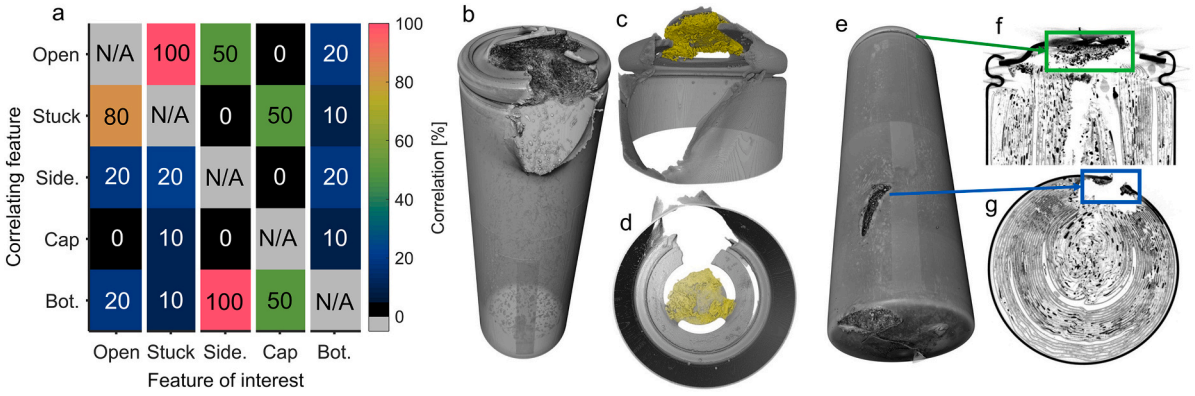


**Fig. 6.** Examination of thermally abused cells. a) Failure mode map for 29 cells tested in relation to this work. Values indicate the appearance frequency (%) of the correlating feature when the feature of interest is present. The feature names are abbreviated from those in Table 2 and are additionally shown in Fig. 7. b)–d) X-ray CT renderings of a carcass (also shown in Fig. 7i) which demonstrated a severe cap rupture, extending some way along the side of the cell. There is an agglomerate of dense material adhered to the inside of the cap, highlighted with a gold colour. e)–g) X-ray CT renderings of a carcass (also shown in Fig. 7a) which demonstrated a sidewall and bottom rupture. The sidewall and bottom ruptures are large, at around 1.2 cm wide, but this does not appear to be sufficient to allow material to leave the cell. As highlighted by the green box in (f), we can again discern an agglomerate of dense material at the cap, which may have occluded it such that material was unable to leave. The blue box in (g) highlights the cell casing at the edge of the rupture, which shows the presence of accumulated material. This suggests that the rupture was created by the melting of the casing, rather than the casing being ripped open due to internal pressure. (For interpretation of the references to colour in this figure legend, the reader is referred to the web version of this article.)

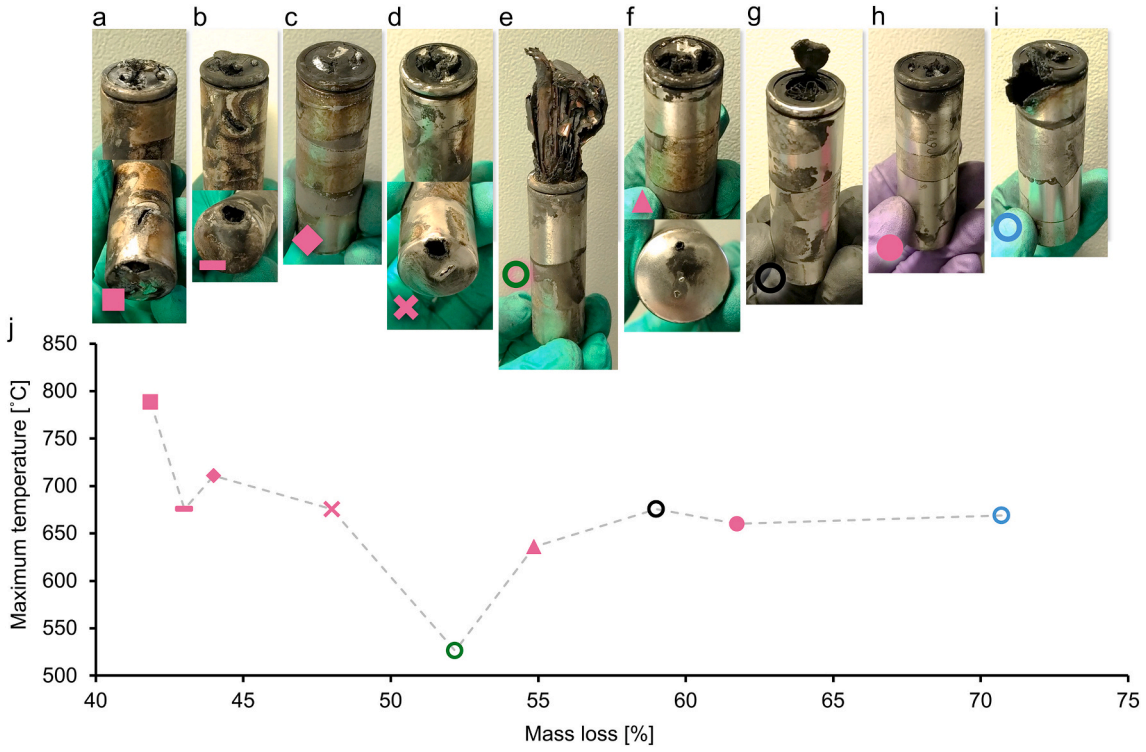


**Fig. 7.** Correlation between the mass lost from cells during thermal runaway and the condition of the cell carcass, as well as the maximum cell surface temperature recorded for each test. The photos show examples of cell carcasses following thermal abuse at 100 % SoC. We observe a broad range of failure modes, including sidewall (a, b) and bottom (a, b, d, f) ruptures, no significant damage (c, h), material stuck in the cap during ejection (e), open cap (g) and cap rupture (i). j) The mass loss and maximum surface temperature reached for each cell; there may be a slight correlation between high maximum temperature and low mass loss. There also appears to be a correlation between low mass loss and sidewall/bottom ruptures.

We examined the dust, which also might be described as soot or black powder, produced during thermal abuse of the test cell using SEM, EDS and air quality monitoring. Dust was collected from the interior of the calorimeter following failure and at least 12 h of cooldown/venting of the system. The dust was removed using a spatula, and any large pieces of debris (e.g., sections of copper current collector or parts of the cell carcass) were discarded as hazardous waste. In some cases, we also found large metal deposits a few cm wide on the calorimeter walls (we assume molten aluminium which had been ejected and solidified after impact, similar to other reports [24]); however, we have not analysed these components in this work. To prepare the SEM samples, dust was pressed onto conductive carbon tape in large quantities, to ensure the surface of the tape was obscured when imaging. Excess dust was tapped off to prevent spillage into the vacuum pump.

The SEM data for the dust are shown in Fig. 8a and b. Here, we can see that the particles produced range in size from hundreds of μm diameter to the order of 1 μm diameter. In particular in Fig. 8b, there is evidence of that some particles may be sub-μm, i.e., 'ultrafine', as has recently been reported for the dust produced during failure testing of NMC and LFP modules [52]. Particles of around 2.5 μm and below (PM2.5) are a known respiratory hazard, capable of long-term physiological damage if inhaled [53]. However, larger diameter particles are still hazardous to health [54,55].

Using EDS, we studied the composition of cell failure dust. As shown in Fig. 8c, the dust is composed of carbon, nickel, aluminium and silicon, with a large contribution from oxygen. This suggests that in addition to carbon particles originating from the anode, and from the incomplete combustion of hydrocarbons, there is a significant contribution from metal particles. Given the high temperatures during thermal runaway and the presence of oxygen, it is very likely that at least some of these are metal oxide particles. The dust that we studied contained significantly smaller particles than those present in failed but intact cathodes [56], but of a comparable size and composition to the dust collected from abuse of lithium nickel manganese cobalt oxide (NMC), i.e., large portions of carbon and metal oxides [57,58]. Most critically, metal oxide particles such as nickel oxide can cause lung inflammation [54] and might have carcinogenic [59] and adverse cardiovascular effects [60]. There are also contributions from fluorine and phosphorus, possibly from organophosphorus and organofluorine compounds remaining on the surface of particles following combustion. Although it is beyond the scope of the present work to fully characterise these materials, it is important to note that the nerve agents sarin and VX are organophosphorus compounds, as are many insecticides, so they are extremely hazardous to health [61]. Organofluorine compounds include many potent greenhouse gases, ozone depleters and persistent organic pollutants, so again this class of chemicals poses a severe environmental and health risk [62].

Finally, to confirm the release of PM2.5 particles during thermal runaway of the test cells, we used a domestic air quality monitor to log the PM2.5 mass fraction locally to the ARC, i.e., leaking from the instrument. As Fig. 8d indicates, less than a minute after the cell enters thermal runaway during a heat ramp test, there is a brief spike in the PM2.5 mass fraction. As described above, exposure to such particles is hazardous to health. Fortunately the time-weighted average of material that we detected falls well below the eight-hour workplace exposure limit of 0.1 mg/m$^3$ [63], but ideally exposure should be entirely avoided. Our system uses robust containment, filtration and local exhaust ventilation to ensure safety; the implication of cell failure in real-world applications outside of such safe conditions is that significant quantities of hazardous material may be released into the environment, and there will be an exposure risk to anyone in the area, in particular emergency service personnel. Such small particles might also be hazardous to local mechanical and electrical equipment, in addition to damage from the heat generated during thermal runaway. These data also imply that proper workplace procedures are essential for safe research into thermal runaway of lithium-ion batteries. Via continual monitoring combined with equipment and procedure refinement, we have fully mitigated particle leakage into the lab from our ARC during abuse testing.

## 4. Conclusions

We have demonstrated that the onset of 0.005 °C/min self-heating may be observed >30 h in advance of thermal runaway, during which time voltage drops also occur. If it were possible to detect self-heating in an individual cell at very small deviations from heating during normal operation, or from voltage drops, then mitigation strategies could be implemented more than a day before thermal runaway. For example, an at-risk pack may be removed from a vehicle, or the individual cell/module might be isolated or neutralised to reduce the risk. Even with lower accuracy measurements, it may be possible to detect and mitigate self-heating minutes or hours before thermal runway. Cells may also leak electrolyte during this time, even before venting. Following venting, there is a delay of a more than an hour before thermal runaway. This leaves a long period during which time gases should be detectable. These results support the conclusions of previous work that gas sensing is an effective method of early detection of thermal runaway, particularly during cell overheating [64]. Notably, carbon dioxide detection has also been validated for batteries undergoing thermal runaway as a result of

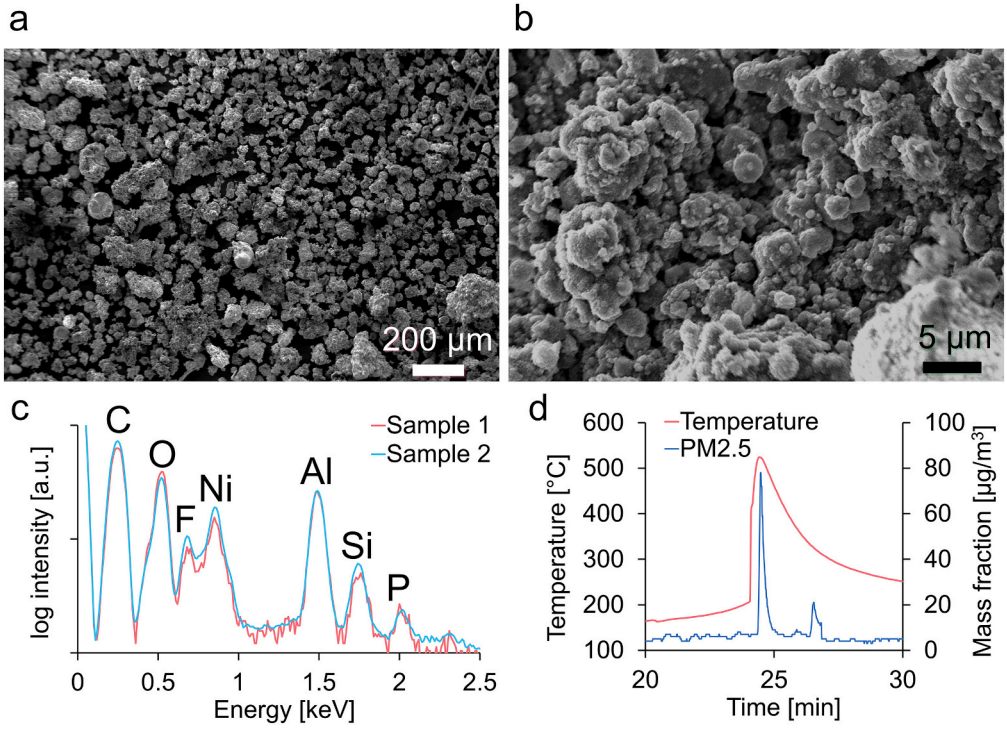


**Fig. 8.** Dust particle analysis from thermal abuse of test cells. a) and b) SEM images of dust samples, demonstrating particles with sizes of hundreds of μm diameter to <1 μm diameter. c) EDS spectra taken from two sample areas, showing the presence of carbon, oxygen and a range of metals present in the cell materials. Phosphorus and fluorine from the lithium salt are also present, along with trace sulphur. d) PM2.5 signal during thermal abuse of a cell at 100 % SoC, showing a measurable quantity of particulate with diameter of 2.5 μm and below around a minute after the cell goes into thermal runaway.

overcharge and internal short circuit [12,13]. There is therefore the potential to implement safety/mitigation strategies based on gas production, such as removing or isolating cells, or moving a battery pack/vehicle to a safe location for further management. Early onset detection is critical in engineering effective safety solutions at the cell, pack and management system level.

During thermal runaway, a range of gaseous species are produced, including $H_2$, $CO_2$, carbonates, carbonate breakdown products and various lighter hydrocarbons. This mixture is highly combustible and toxic due to the presence of aromatic species. The debris produced by cell failure poses an additional and significant carcinogenic risk, due to the presence of PM2.5 dust containing metal and metal oxide particles. These particulates might also pose a risk to other critical systems (e.g., electronic, mechanical) that could be damaged by dust ingress, resulting in cumulative hazards (for example, if a navigation system was compromised by dust damage). Altogether, the material produced by failing cells is extremely hazardous to health; research must be carried out safely, and failure events in the real world must be handled such that the risk to emergency service personnel, the public and the environment is minimised.

We have observed that the study cell tends to rupture during thermal runaway. This appears to be correlated with the behaviour of the cap and, as such, the mass lost from the cell. Cells will typically rupture if the contents are unable to eject to relieve pressure, which limits thermal dissipation and the removal of combustible material. This increases the severity of failure; in the context of battery pack design, a rupturing cell poses a high risk of propagating thermal runaway to its neighbours. Therefore, it is critical to minimise the chance of rupturing via engineering solutions at the cell, pack and battery management levels. For example, the study cells were mandrel-free, but in other work the mandrel appears to help with opening the cap so material can eject effectively [65]. It may also be worth considering strategies such as making the cap or rill weaker, so that the cell can more easily open in the event of failure.

Finally, we emphasise that our methodology in this work is applicable to cells of nominally any geometry and/or chemistry. Our approach forms a robust assessment of cell failure, coupling techniques to produce a broad overview of the study cell. This highlights the expectation of how it will behave under failure conditions, the likely best- and worst-case scenarios for failure, and how the resulting hazards would be expected to have an effect in real-world scenarios.

Supplementary data to this article can be found online at https://doi.org/10.1016/j.est.2023.107069.

## CRediT authorship contribution statement

**Mark Buckwell:** Conceptualization, Methodology, Validation, Formal analysis, Investigation, Writing – original draft, Writing – review & editing, Visualization. **Charlie Kirchner-Burles:** Investigation. **Rhodri E. Owen:** Methodology, Formal analysis, Writing – review & editing. **Tobias P. Neville:** Methodology, Formal analysis, Writing – review & editing. **Julia S. Weaving:** Methodology, Writing – review & editing, Project administration. **Daniel J.L. Brett:** Supervision, Project administration, Funding acquisition. **Paul R. Shearing:** Conceptualization, Writing – review & editing, Supervision, Project administration, Funding acquisition.

## Declaration of competing interest

The authors declare that they have no known competing financial interests or personal relationships that could have appeared to influence the work reported in this paper.

## Data availability

Data will be made available on request.

## Acknowledgements

This work was supported by the Faraday Institution (Faraday.ac.uk; EP/S003053/1, grant number FIRG028), as well as the National Physical Laboratory and the Engineering and Physical Sciences Council (EP/V519623/1). P. R. S. acknowledges funding from the Royal Academy of Engineering (CiET1718\59), as does D. J. L. B. (RCSRF2021/13/53).

## References

[1] D. Doughty, E.P. Roth, A general discussion of Li ion battery safety, Electrochem. Soc. Interface 21 (2012) 37–44, https://doi.org/10.1149/2.F03122if.
[2] D.P. Finegan, X-ray Imaging of Failure and Degradation Mechanisms of Lithium-ion Batteries, 2016, https://doi.org/10.1017/CBO9781107415324.004.
[3] J. Xu, H.R. Thomas, R.W. Francis, K.R. Lum, J. Wang, B. Liang, A review of processes and technologies for the recycling of lithium-ion secondary batteries, J. Power Sources 177 (2008) 512–527, https://doi.org/10.1016/j.jpowsour.2007.11.074.
[4] A.R. Baird, E.J. Archibald, K.C. Marr, O.A. Ezekoye, Explosion hazards from lithium-ion battery vent gas, J. Power Sources 446 (2020), 227257, https://doi.org/10.1016/j.jpowsour.2019.227257.
[5] M. Onuki, S. Kinoshita, Y. Sakata, M. Yanagidate, Y. Otake, M. Ue, M. Deguchi, Identification of the source of evolved gas in Li-ion batteries using 13C-labeled solvents, J. Electrochem. Soc. 155 (2008) A794, https://doi.org/10.1149/1.2969947.
[6] P. Ribière, S. Grugeon, M. Morcrette, S. Boyanov, S. Laruelle, G. Marlair, Investigation on the fire-induced hazards of li-ion battery cells by fire calorimetry, Energy Environ. Sci. 5 (2012) 5271–5280, https://doi.org/10.1039/c1ee02218k.
[7] T. Kawamura, A. Kimura, M. Egashira, S. Okada, J.I. Yamaki, Thermal stability of alkyl carbonate mixed-solvent electrolytes for lithium ion cells, J. Power Sources 104 (2002) 260–264, https://doi.org/10.1016/S0378-7753(01)00960-0.
[8] A. Daniano, M. Porru, A. Salimbeni, A. Serpi, V. Castiglia, A.O.Di Tomaso, R. Miceli, G. Shettino, Batteries for aerospace: a breif review, in: IEE 2018 AEIT Int. Annu. Conf, 2018.
[9] L. Lao, Y. Su, Q. Zhang, S. Wu, Thermal Runaway Induced Casing Rupture : Formation Mechanism and Effect on Propagation in Cylindrical Lithium Ion Battery Module Thermal Runaway Induced Casing Rupture : Formation Mechanism and Effect on Propagation in Cylindrical Lithium Ion Battery Modu, 2020, https://doi.org/10.1149/1945-7111/ab8807.
[10] N.S. Spinner, C.R. Field, M.H. Hammond, B.A. Williams, K.M. Myers, A.L. Lubrano, S.L. Rose-Pehrsson, S.G. Tuttle, Physical and chemical analysis of lithium-ion battery cell-to-cell failure events inside custom fire chamber, J. Power Sources 279 (2015) 713–721, https://doi.org/10.1016/j.jpowsour.2015.01.068.
[11] M. Brand, S. Gläser, J. Geder, S. Menacher, S. Obpacher, A. Jossen, D. Quinger, Electrical safety of commercial li-ion cells based on NMC and NCA technology compared to LFP technology, World Electr. Veh. J. 6 (2013) 572–580, https://doi.org/10.3390/wevj6030572.
[12] T. Cai, P. Mohtat, A.G. Stefanopoulou, J.B. Siegel, Li-ion battery fault detection in large packs using force and gas sensors, IFAC-PapersOnLine. 53 (2020) 12491–12496, https://doi.org/10.1016/j.ifacol.2020.12.1763.
[13] T. Cai, P. Valecha, V. Tran, B. Engle, A. Stefanopoulou, J. Siegel, Detection of li-ion battery failure and venting with carbon dioxide sensors, ETransportation. 7 (2021), 100100, https://doi.org/10.1016/j.etran.2020.100100.
[14] A. Ibrahim, F. Jiang, The electric vehicle energy management: an overview of the energy system and related modeling and simulation, Renew. Sust. Energ. Rev. 144 (2021), 111049, https://doi.org/10.1016/j.rser.2021.111049.
[15] P. Tol, Qualitative colour schemes, Paul Tol's Notes Colour Schemes Templates. https://personal.sron.nl/~pault/, 2021 (accessed March 1, 2022).
[16] jdherman, Colormap. https://github.com/jdherman/colormap, 2015.
[17] E.P. Roth, D.H. Doughty, Thermal abuse performance of high-power 18650 Li-ion cells, J. Power Sources 128 (2004) 308–318, https://doi.org/10.1016/j.jpowsour.2003.09.068.
[18] M.N. Richard, J.R. Dahn, Accelerating rate calorimetry study on the thermal stability of lithium intercalated graphite in electrolyte. II. Modeling the results and predicting differential scanning calorimeter curves, J. Electrochem. Soc. 146 (1999) 2078–2084, https://doi.org/10.1149/1.1391894.
[19] C. Lampe-Onnerud, J. Shi, R. Chamberlain, P. Onnerud, Safety studies of Li-ion key components by ARC, Proc. Annu. Batter. Conf. Appl. Adv. (2001) 367–374, https://doi.org/10.1109/bcaa.2001.905156.
[20] D.D. MacNeil, D. Larcher, J.R. Dahn, Comparison of the reactivity of various carbon electrode materials with electrolyte at elevated temperature, J. Electrochem. Soc. 146 (1999) 3596–3602, https://doi.org/10.1149/1.1392520.
[21] B. Lei, W. Zhao, C. Ziebert, N. Uhlmann, M. Rohde, H.J. Seifert, Experimental analysis of thermal runaway in 18650 cylindrical Li-ion cells using an accelerating rate calorimeter, Batteries 3 (2017) 1–14, https://doi.org/10.3390/batteries3020014.
[22] A.V. Shelkea, J.E.H. Buston, J. Gill, D. Howard, R.C.E. Williams, E. Read, A. Abaza, B. Cooper, P. Richards, J.X. Wen, Combined numerical and experimental studies of 21700 lithium-ion battery thermal runaway induced by different thermal abuse, Int. J. Heat Mass Transf. 194 (2022), 123099, https://doi.org/10.1016/j.ijheatmasstransfer.2022.123099.

[23] K. Chiba, A. Yoshizawa, Y. Isogai, Thermal safety diagram for lithium-ion battery using single-crystal and, J. Energy Storage 32 (2020), 101775, https://doi.org/10.1016/j.est.2020.101775.
[24] M.S. Md Said, M.Z. Mohd Tohir, Characterisation of thermal runaway behaviour of cylindrical lithium-ion battery using accelerating rate calorimeter and oven heating, case stud, Therm. Eng. 28 (2021), 101474, https://doi.org/10.1016/j.csite.2021.101474.
[25] C.Y. Jhu, Y.W. Wang, C.M. Shu, J.C. Chang, H.C. Wu, Thermal explosion hazards on 18650 lithium ion batteries with a VSP2 adiabatic calorimeter, J. Hazard. Mater. 192 (2011) 99–107, https://doi.org/10.1016/j.jhazmat.2011.04.097.
[26] R. Spotnitz, J. Franklin, Abuse behavior of high-power, lithium-ion cells, J. Power Sources 113 (2003) 81–100, https://doi.org/10.1016/S0378-7753(02)00488-3.
[27] G. Venugopal, Characterization of thermal cut-off mechanisms in prismatic lithium-ion batteries, J. Power Sources 101 (2001) 231–237, https://doi.org/10.1016/S0378-7753(01)00782-0.
[28] J.S. Gnanaraj, E. Zinigrad, L. Asraf, H.E. Gottlieb, M. Sprecher, D. Aurbach, M. Schmidt, The use of accelerating rate calorimetry (ARC) for the study of the thermal reactions of Li-ion battery electrolyte solutions, J. Power Sources 119–121 (2003) 794–798, https://doi.org/10.1016/S0378-7753(03)00255-6.
[29] G. Zhang, X. Wei, S. Chen, J. Zhu, G. Han, X. Wang, H. Dai, Revealing the impact of fast charge cycling on the thermal safety of lithium-ion batteries, ACS Appl. Energy Mater. (2022), https://doi.org/10.1021/acsaem.2c00688.
[30] K. Xu, Nonaqueous liquid electrolytes for lithium-based rechargeable batteries, ChemInform 35 (2004), https://doi.org/10.1002/chin.200450271.
[31] K. Liu, Y. Liu, D. Lin, A. Pei, Y. Cui, Materials for lithium-ion battery safety, Sci. Adv. 4 (2018), https://doi.org/10.1126/sciadv.aas9820.
[32] J. Lamb, C.J. Orendorff, E.P. Roth, J. Langendorf, Studies on the thermal breakdown of common li-ion battery electrolyte components, J. Electrochem. Soc. 162 (2015) A2131–A2135, https://doi.org/10.1149/2.0651510jes.
[33] Z. Zhang, D. Fouchard, J.R. Rea, Differential scanning calorimetry material studies: implications for the safety of lithium-ion cells, J. Power Sources 70 (1998) 16–20, https://doi.org/10.1016/S0378-7753(97)02611-6.
[34] M. Holzapfel, A. Würsig, W. Scheifele, J. Vetter, P. Novák, Oxygen, hydrogen, ethylene and CO2 development in lithium-ion batteries, J. Power Sources 174 (2007) 1156–1160, https://doi.org/10.1016/j.jpowsour.2007.06.182.
[35] A. Du Pasquier, F. Disma, T. Bowmer, A.S. Gozdz, G. Amatucci, J.-M. Tarascon, Differential scanning calorimetry study of the reactivity of carbon anodes in plastic Li-ion batteries, J. Electrochem. Soc. 145 (1998) 472, https://doi.org/10.1149/1.1838287.
[36] NIST, NIST Standard Reference Database Number 69, Chem. Webb, 2022, https://doi.org/10.18434/T4D303.
[37] H. Yoshida, T. Fukunaga, T. Hazama, M. Terasaki, M. Mizutani, M. Yamachi, Degradation mechanism of alkyl carbonate solvents used in lithium-ion cells during initial charging, J. Power Sources 68 (1997) 311–315, https://doi.org/10.1016/S0378-7753(97)02635-9.
[38] T. Sasaki, T. Abe, Y. Iriyama, M. Inaba, Z. Ogumi, Formation mechanism of alkyl dicarbonates in li-ion cells, J. Power Sources 150 (2005) 208–215, https://doi.org/10.1016/j.jpowsour.2005.02.021.
[39] S.E. Sloop, J.B. Kerr, K. Kinoshita, The role of li-ion battery electrolyte reactivity in performance decline and self-discharge, J. Power Sources 119–121 (2003) 330–337, https://doi.org/10.1016/S0378-7753(03)00149-6.
[40] R. Petibon, L. Rotermund, K.J. Nelson, A.S. Gozdz, J. Xia, J.R. Dahn, Study of electrolyte components in li ion cells using liquid-liquid extraction and gas chromatography coupled with mass spectrometry, J. Electrochem. Soc. 161 (2014) A1167–A1172, https://doi.org/10.1149/2.117406jes.
[41] S.E. Sloop, J.K. Pugh, S. Wang, J.B. Kerr, K. Kinoshita, Chemical reactivity of PF5 and LiPF6 in ethylene carbonate/dimethyl carbonate solutions, Electrochem. Solid-State Lett. 4 (2001) 6–7, https://doi.org/10.1149/1.1353158.
[42] J.C. Gentry, Benzene production and economics: a review, Asia Pac. J. Chem. Eng. 2 (2007) 272–277, https://doi.org/10.1002/apj.018.
[43] C.L. Campion, W. Li, B.L. Lucht, Thermal decomposition of LiPF[sub 6]-based electrolytes for lithium-ion batteries, J. Electrochem. Soc. 152 (2005) A2327, https://doi.org/10.1149/1.2083267.
[44] D.P. Abraham, E.P. Roth, R. Kostecki, K. McCarthy, S. MacLaren, D.H. Doughty, Diagnostic examination of thermally abused high-power lithium-ion cells, J. Power Sources 161 (2006) 648–657, https://doi.org/10.1016/j.jpowsour.2006.04.088.
[45] A. Reizian, Y. Dat, S. Rault, M. Robba, Mass spectral study of chlorofluorocarbons (CFCs) and potential alternatives (HCFCs and HFCs), Ecotoxicol. Environ. Saf. 29 (1994) 47–60, https://doi.org/10.1016/0147-6513(94)90029-9.
[46] A.W. Golubkov, S. Scheikl, R. Planteu, G. Voitic, H. Wiltsche, C. Stangl, G. Fauler, A. Thaler, V. Hacker, Thermal runaway of commercial 18650 Li-ion batteries with LFP and NCA cathodes - impact of state of charge and overcharge, RSC Adv. 5 (2015) 57171–57186, https://doi.org/10.1039/c5ra05897j.
[47] X. Feng, S. Zheng, D. Ren, X. He, L. Wang, H. Cui, X. Liu, C. Jin, F. Zhang, C. Xu, H. Hsu, S. Gao, T. Chen, Investigating the thermal runaway mechanisms of lithium-ion batteries based on thermal analysis database, Appl. Energy 246 (2019) 53–64, https://doi.org/10.1016/j.apenergy.2019.04.009.
[48] W.Q. Walker, J.J. Darst, D.P. Finegan, G.A. Bayles, K.L. Johnson, E.C. Darcy, S. L. Rickman, Decoupling of heat generated from ejected and non-ejected contents of 18650-format lithium-ion cells using statistical methods, J. Power Sources 415 (2019) 207–218, https://doi.org/10.1016/j.jpowsour.2018.10.099.
[49] C.M.R. Vendra, A.V. Shelke, J.E.H. Buston, J. Gill, D. Howard, E. Read, A. Abaza, B. Cooper, J.X. Wen, Numerical and experimental characterisation of high energy density 21700 lithium-ion battery fires, Process Saf. Environ. Prot. 160 (2022) 153–165, https://doi.org/10.1016/j.psep.2022.02.014.
[50] D.P. Finegan, M. Scheel, J.B. Robinson, B. Tjaden, I. Hunt, T.J. Mason, J. Millichamp, M. Di Michiel, G.J. Offer, G. Hinds, D.J.L. Brett, P.R. Shearing, In-operando high-speed tomography of lithium-ion batteries during thermal runaway, Nat. Commun. 6 (2015) 1–10, https://doi.org/10.1038/ncomms7924.
[51] D.P. Finegan, B. Tjaden, T.M.M. Heenan, R. Jervis, M. Di Michiel, A. Rack, G. Hinds, D.J.L. Brett, P.R. Shearing, Tracking internal temperature and structural dynamics during nail penetration of lithium-ion cells, J. Electrochem. Soc. 164 (2017) A3285–A3291, https://doi.org/10.1149/2.1501713jes.
[52] V. Premnath, Y. Wang, N. Wright, I. Khalek, S. Uribe, Detailed characterization of particle emissions from battery fires, Aerosol Sci. Technol. 56 (2022) 337–354, https://doi.org/10.1080/02786826.2021.2018399.
[53] G.D. Thurston, R.T. Burnett, M.C. Turner, Y. Shi, D. Krewski, R. Lall, K. Ito, M. Jerrett, S.M. Gapstur, W. Ryan Diver, C. Arden Pope, Ischemic heart disease mortality and long-term exposure to source-related components of U.S. fine particle air pollution, Environ. Health Perspect. 124 (2016) 785–794, https://doi.org/10.1289/ehp.1509777.
[54] K. Styszko, L. Samek, K. Szramowiat, A. Korzeniewska, K. Kubisty, R. Rakoczy-Lelek, M. Kistler, A.K. Giebl, Oxidative potential of PM10 and PM2.5 collected at high air pollution site related to chemical composition: Krakow case study, Air Qual. Atmos. Heal. 10 (2017) 1123–1137, https://doi.org/10.1007/s11869-017-0499-3.
[55] E. Samoli, R.W. Atkinson, A. Analitis, G.W. Fuller, D. Beddows, D.C. Green, I. S. Mudway, R.M. Harrison, H.R. Anderson, F.J. Kelly, Differential health effects of short-term exposure to source-specific particles in London, U.K, Environ. Int. 97 (2016) 246–253, https://doi.org/10.1016/j.envint.2016.09.017.
[56] D. Patel, J.B. Robinson, S. Ball, D.J.L. Brett, P.R. Shearing, Thermal runaway of a li-ion battery studied by combined ARC and multi-length scale X-ray CT, J. Electrochem. Soc. 167 (2020), 090511, https://doi.org/10.1149/1945-7111/ab7fb6.
[57] S. Chen, Z. Wang, W. Yan, Identification and characteristic analysis of powder ejected from a lithium ion battery during thermal runaway at elevated temperatures, J. Hazard. Mater. 400 (2020), 123169, https://doi.org/10.1016/j.jhazmat.2020.123169.
[58] T.L. Barone, T.H. Dubaniewicz, S.A. Friend, I.A. Zlochower, A.D. Bugarski, N. S. Rayyan, Lithium-ion battery explosion aerosols: morphology and elemental composition, Aerosol Sci. Technol. 55 (2021) 1183–1201, https://doi.org/10.1080/02786826.2021.1938966.
[59] M. Yu, J. Zhang, Serum and hair nickel levels and breast cancer: systematic review and meta-analysis, Biol. Trace Elem. Res. 179 (2017) 32–37, https://doi.org/10.1007/s12011-017-0949-7.
[60] M. Lippmann, K. Ito, J.S. Hwang, P. Maciejczyk, L.C. Chen, Cardiovascular effects of nickel in ambient air, Environ. Health Perspect. 114 (2006) 1662–1669, https://doi.org/10.1289/ehp.9150.
[61] R.A. Lewis, Lewis' dictionary of toxicology, in: Lewis' Dict. Toxicol, 1st ed., CRC Press, 1998, p. 763.
[62] D.M. Lemal, Perspective on fluorocarbon chemistry, J. Org. Chem. 69 (2004) 1–11, https://doi.org/10.1021/jo0302556.
[63] HSE, EH40/2005 Workplace Exposure Limits, 4th ed., TSO, London, 2020. https://www.hse.gov.uk/pubns/books/eh40.htm.
[64] C. Essl, L. Seifert, M. Rabe, A. Fuchs, Early detection of failing automotive batteries using gas sensors, Batteries 7 (2021), https://doi.org/10.3390/batteries7020025.
[65] D.P. Finegan, E. Darcy, M. Keyser, B. Tjaden, T.M.M. Heenan, R. Jervis, J.J. Bailey, N.T. Vo, O.V. Magdysyuk, M. Drakopoulos, M. Di Michiel, A. Rack, G. Hinds, D.J. L. Brett, P.R. Shearing, Identifying the cause of rupture of Li-ion batteries during thermal runaway, Adv. Sci. 5 (2018), https://doi.org/10.1002/advs.201700369.